

Magnetic structure of Sm_2IrIn_8

C. Adriano,^{1,*} R. Lora-Serrano,¹ C. Giles,¹ F. de Bergevin,² J. C. Lang,³ G. Srajer,³ C. Mazzoli,² L. Paolasini,² and P. G. Pagliuso¹

¹*Instituto de Física "Gleb Wataghin", UNICAMP, 13083-970, Campinas-São Paulo, Brazil.*

²*European Synchrotron Radiation Facility, Grenoble 38043, France.*

³*Advanced Photon Source, Argonne National Laboratory, Argonne, Illinois 60439.*

(Dated: December 28, 2018)

The magnetic structure of the intermetallic antiferromagnet Sm_2IrIn_8 was determined using x-ray resonant magnetic scattering (XRMS). Below $T_N = 14.2$, Sm_2IrIn_8 has a commensurate antiferromagnetic structure with a propagation vector $\vec{\eta} = (1/2, 0, 0)$. The Sm magnetic moments lie in the ab plane and are rotated roughly 18° away from the a axis. The magnetic structure of this compound was obtained by measuring the strong dipolar resonant peak whose enhancement was of over two orders of magnitude at the L_2 edge. At the L_3 edge both quadrupolar and dipolar features were observed in the energy line shape. The magnetic structure and properties of Sm_2IrIn_8 are found to be consistent with the general trend already seen for the Nd-, Tb- and the Ce-based compounds from the $\text{R}_m\text{M}_n\text{In}_{3m+2n}$ family ($\text{R} = \text{rare earth}$; $\text{M} = \text{Rh or Ir}$, $m = 1, 2$; $n = 0, 1$), where the crystalline electrical field (CEF) effects determine the direction of magnetic moments and the T_N evolution in the series. The measured Néel temperature for Sm_2IrIn_8 is slightly suppressed when compared to the T_N of the parent cubic compound SmIn_3 .

PACS numbers: 75.25.+z, 75.50.Ee, 75.30.-m, 75.30.Kz

I. INTRODUCTION

The microscopic details of $4f$ -electron magnetism play a fundamental role in the physical properties of various classes of rare-earth based materials such as heavy fermions, magnetically ordered alloys and permanent magnets. The existence of structurally related families of rare-earth based compounds provides a great opportunity to explore how the details of the $4f$ -electrons magnetism evolve as a function of changes in the dimensionality, local symmetry and electronic structure along each related family. The recently discovered^{1,2,3,4,5,6,7,8} family of intermetallic compounds $\text{R}_m\text{M}_n\text{In}_{3m+2n}$ ($\text{M} = \text{Co, Rh or Ir}$, $m = 1, 2$; $\text{R} = \text{La, Ce, Pr, Nd, Sm, Gd}$) have proved to be very promising in this regard, since it possesses many members of structurally related heavy-fermions superconductors (HFS), for $\text{R} = \text{Ce}$, antiferromagnets ($\text{R} = \text{Nd, Sm, Gd and Tb}$) and paramagnetic metals ($\text{R} = \text{La, Pr}$). Within this family, the physical properties of a particular R-member can also be compared to compounds based on the same R with three different related structures [the cubic RIn_3 and the tetragonal $\text{RMIn}_5(1-1-5)$ and $\text{R}_2\text{MIn}_8(2-1-8)$ ^{9,10,11} and/or to the same R formed with three distinct transition metals ($\text{M} = \text{Rh, Ir and Co}$ - not for all R -) in the same structure.

For the Ce-based HFS in this family, extensive investigation has revealed fascinating physical properties such as quantum criticality, non-fermi-liquid-behavior and an intriguing interplay between magnetism and superconductivity, reflected in very rich phase diagrams.^{12,13,14,15,16,17,18,19,20} Because the HFS members of this family are structurally related, its investigation has been used to provide some insights on the question why some structure types are favorable to host many superconductors. A possible relationship between the su-

perconducting critical temperature T_c and the crystalline anisotropy^{13,21,22}, the role of the $4f$ -electron hybridization with the conduction electrons in the occurrence of superconductivity^{23,24,25} and the effects of quasi-2D electronics structures^{26,27,28} are some of the physical phenomena that have been brought to the scenario to answer the question above. Further, motivated by this experimental trend, new materials search based on the 1-1-5 structures has led to the discovery of the Pu-based HFS PuMGa_5 ($\text{M} = \text{Rh and Co}$).^{29,30}

On the other hand, as these HFS are presumably magnetically mediated, others studies^{5,6,7,21,31,32,33,34,35,36,37} have been focused in understanding the evolution of the $4f$ local magnetism, not only for the magnetically ordered Ce-based members of this family such as CeRhIn_5 and Ce_2RhIn_8 , but also for their antiferromagnetic counterparts $\text{R}_m\text{M}_n\text{In}_{3m+2n}$ ($\text{M} = \text{Rh or Ir}$, $m = 1, 2$;) for $\text{R} = \text{Nd, Sm, Gd and Tb}$. From these studies, it was established the role of tetragonal crystalline electrical field (CEF) in determining the spatial direction of the ordered R-moments with respect to the lattice and the evolution of the Néel temperature, T_N , in the series.^{5,6,7,32,37}

A key set of experiments allowing the above conclusions was the experimental determination of the magnetic structures of various members of the $\text{R}_m\text{M}_n\text{In}_{3m+2n}$ ($\text{M} = \text{Rh or Ir}$, $m = 1, 2$;) family.^{7,31,36,38,39,40,41} Up to date, however, none of the Sm-based compounds from this family have had their magnetic structures determined. In fact, the compounds of this series containing Sm ions may be particularly important in testing the extension of the CEF trends in this family because the presence of excited J -multiplet states in Sm^{3+} and quadrupolar interactions have to be taken into account in order to understand their magnetic phase diagrams.^{42,43,44,45} Especially interesting is Sm_2IrIn_8 which presents a first or-

der antiferromagnetic transition at $T_N = 14.2$ K.⁵ This value is slightly smaller than the $T_N \sim 16$ K of the cubic SmIn_3 ¹¹ which according to the CEF trends observed in other members of this family^{7,37} suggest that the ordered Sm-moments should lie the ab -plane.

To further explore the magnetic properties of Sm_2IrIn_8 and to check the extension of the CEF trends observed for $R = \text{Nd, Tb, and Ce}$,^{5,6,7,32,37} to the Sm-based compounds, we report in this work the solution of the magnetic structure of the intermetallic antiferromagnet Sm_2IrIn_8 by means of the x-ray resonant magnetic scattering (XRMS) technique. The XRMS technique has proved to be a very important tool for the investigation of microscopic magnetism in condensed matter, specially for highly neutrons absorber ions such as Sm.

Sm_2IrIn_8 presents, below $T_N = 14.2$ K, a commensurate antiferromagnetic structure with a propagation vector $\vec{\eta} = (\frac{1}{2}, 0, 0)$. The Sm magnetic moments lie in the ab plane. In terms of relative orientation, the propagation vector $\vec{\eta}$ indicates that the Sm-spins are ordered antiferromagnetically along the a axis and ferromagnetically along the b axis and, because of the presence of two Sm ions per unit cell along c axis, some calculations have to be performed in order to determine the type of ordering along this direction. Furthermore, as it could be expected for such spin arrangement in a tetragonal compound, antiferromagnetic domains were observed in the ordered state of Sm_2IrIn_8 . These domains were removed by field-cooling the sample at a field of $H = 10$ T.

II. EXPERIMENT

Single crystalline samples of Sm_2IrIn_8 were grown from Indium flux as described previously.^{5,46} The crystal structure, unit cell dimensions and macroscopic properties of the Sm_2IrIn_8 single crystals used in this work were in agreement with the data in Ref. 5. For the XMRS experiments of this work, selected crystals were extracted and prepared with polished $(0,0,l)$ flat surfaces, and sizes of approximately 4 mm x 3.4 mm x 1.5 mm. The preferred crystal growth direction of this tetragonal compound is columnar along the $[00l]$ direction and the (001) facet is relatively large. The mosaic spread of the sample was found to be $< 0.08^\circ$ by a rocking curve (θ scan) on a Phillips four circle diffractometer.

XRMS studies were performed at the 4-ID-D beamline at the Advanced Photon Source (APS) and at the ID-20 beamline at the European Synchrotron Radiation Facility (ESRF). The 4-ID-D x-ray source is a 33 mm period planar undulator and the energy is selected with a double crystal Si(111) monochromator. A toroidal mirror focuses the beam to a $220 \mu\text{m}$ (horizontal) x $110 \mu\text{m}$ (vertical) spot, yielding an incident flux of $\sim 3.5 \times 10^{13}$ photons/s with an energy resolution of $\delta E/E = 1.4 \times 10^{-4}$. The sample was cooled in a closed-cycle He refrigerator (with a base temperature of 4 K) with a dome Be window. Our experiments were performed in the copla-

nar geometry with σ -polarized incident photons, i.e., in the vertical scattering plane, using a four-circle diffractometer. Except for azimuthal scans, the sample was mounted with the b axis perpendicular to the scattering plane.

In most measurements, we have performed a polarization analysis, with Cu(220), Graphite (006) and Au(111) crystal analysers, appropriate for the energies of Sm L_2 and L_3 edges. The diffractometer configuration at the APS allowed measurements at different azimuthal angles (ϕ) by rotating the sample around the scattering vector \mathbf{Q} . This was particularly useful to probe the magnetic moment components at the dipolar resonant condition with σ incident polarization.

The x-ray source on the ID-20 beamline was a linear undulator with a 32 mm period. The main optical components are a double Si(111) crystal monochromator with sagittal focusing and two meridional focusing mirrors on either side of the monochromator. At 7.13 keV using the first harmonic of the undulator u32, the standard incident flux at the sample position was approximately 1×10^{13} ph/s at 200 mA with a beam size of $500 \mu\text{m}$ (horizontal) x $400 \mu\text{m}$ (vertical). The sample was mounted on a cryomagnet (with a base temperature of 2 K), installed on a horizontal six-circle diffractometer, with the b axis parallel to the cryomagnet axis and perpendicular to the scattering plane. This configuration allowed π -polarized incident photons in the sample and the application of an external magnetic field up to 10 T perpendicular to the scattering plane.

III. RESULTS

A. Temperature dependence and resonance analysis

Magnetic peaks were observed in the dipolar resonant condition at temperatures below $T_N = 14.2$ K at reciprocal lattice points forbidden for charge scattering and consistent with an antiferromagnetic structure with propagation vector $(\frac{1}{2}, 0, 0)$. Their temperature dependence was studied for increasing and decreasing temperature sweeps. Figure 1 shows the temperature dependence of $(0, \frac{1}{2}, 9)$ magnetic reflection at an incident photon energy of 7.313 keV (L_2 edge) and measured at π incident polarization without polarization analysis. The squared root of the integrated intensity, which is proportional to a Sm sub-lattice magnetization, is displayed. A pseudo-voigt peak shape was used to fit transversal θ scans through the reciprocal lattice points in order to obtain the integrated intensities of the reflection peak. This peak intensity decreases abruptly to zero for $T > 13$ K and its critical behavior can not be described by a power-law function with a critical exponent β . This result is in agreement with the first order character of the magnetic transition at 14.2 K, revealed by heat capacity data, from which a latent heat of ~ 10 J/mol was extracted.⁵ Consistently, we found

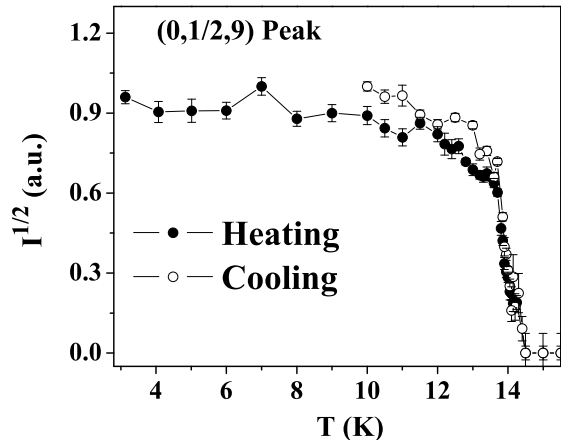


FIG. 1: Temperature dependence of one Sm_2IrIn_8 sub-lattice magnetization measured with transverse (θ) scans at the $(0, \frac{1}{2}, 9)$ peak.

evidence of small hysteresis for $T \lesssim 14.2$ when changing from warming to the cooling temperature sweep.

The energy line shape curves for the polarization channels $\sigma - \pi'$ and $\sigma - \sigma'$ of the $(\frac{1}{2}, 0, 9)$ diffraction peak at (a) the L_2 and (b) the L_3 absorption edges of Sm^{3+} ion at $T = 5.9$ K are shown in Figure 2. The solid lines in both panels represent the absorption spectrum, $\mu(E)$, extracted from fluorescence yield. The data of Figure 2 were collected at the 4-ID-D beamline of APS by counting the photons reaching the detector at a fixed \mathbf{Q} while changing the incident energy. The strong resonant enhancement of the x-ray scattering at this reciprocal space position provide clear evidence of the magnetic origin of the observed peaks.

The energy scan curve in Figure 2(a) has a maximum at 7.312 keV which is only ~ 2.5 eV larger than the L_2 absorption edge (defined by the inflection point of the absorption spectrum), revealing the electric dipolar character ($E1$) of this transition (from $2p$ to $5d$ states). Figure 2 also shows the polarization analysis performed to unambiguously confirm the magnetic origin of the superstructure peaks. Polarization analysis was also used to verify whether the anomaly at approximately 8 eV below the dipolar peak in Figure 2(a) could be associated with a quadrupolar transition⁴⁷ or it simply represents an enhanced interference between the non-resonant and the resonant part of the scattering amplitude. For the experimental configuration used (incident σ -polarization), the electric dipole transitions $E1$ rotate the plane of polarization into the scattering plane (π -polarization). Our data in Figure 2(a) reveals a strong enhancement of the scattered intensities at the $\sigma - \pi'$ channel (closed circles) and no enhancement at the $\sigma - \sigma'$ channel for the same energy range. These results confirm the magnetic origin of the $(h, 0, l) \pm (\frac{1}{2}, 0, 0)$ reflections due to the ex-

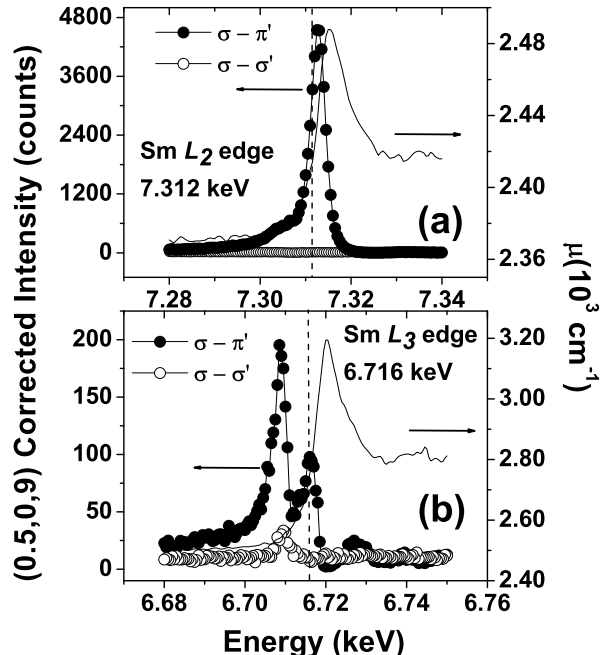


FIG. 2: Energy scan of the $(\frac{1}{2}, 0, 9)$ magnetic peak at $T = 5.9$ K for $\sigma - \pi'$ (closed circles) and $\sigma - \sigma'$ (open circles) polarization channels at the L_2 (top) and L_3 (bottom) absorption edges. The data have been corrected for absorption, $\mu(E)$, using the measured fluorescence yield. Arrows indicate the scales for the fluorescence yield (right) and the observed data (left).

istence of an antiferromagnetic structure doubled along the crystallographic \hat{a} direction, with a propagation vector $\vec{\eta} = (\frac{1}{2}, 0, 0)$.

The energy profile around the $\text{Sm } L_3$ edge is presented in Figure 2(b). Firstly, the observed intensities are roughly one order of magnitude weaker than those obtained at the L_2 resonance, in agreement with previous measurements on pure Sm .⁴⁵ Secondly, there are two peaks in the $\sigma - \pi'$ channel signal, as also observed for other light rare-earth^{48,49} and Sm -based compounds.^{45,50} A high energy peak appears at 6.716 keV, while a low energy and more intense enhancement can be observed at 6.708 keV. Interestingly, Stunault *et al.*⁴⁵ have demonstrated that for pure Sm the quadrupolar $E2$ resonance is more intense than the dipolar $E1$ at the L_3 edge and they found that the energy difference between the $E2$ and the $E1$ resonances is of the order of 8 eV, the same as the one found in this work. Furthermore, in the $\sigma - \sigma'$ channel only an enhancement at 6.708 keV could be observed which is consistent with the quadrupolar character of this resonance, since scattering signal in $\sigma - \sigma'$ channel for dipolar transitions is strictly forbidden.^{47,51} Thus, the presence of this pre-edge enhancement in the energy curves of Figure 2 confirms an expected quadrupole ($E2$) $2p$ to $4f$ contribution to the resonant x-ray scattering in

Sm₂IrIn₈.

B. The magnetic structure

The magnetic structure of the Sm₂IrIn₈ was experimentally investigated using dipolar resonant x-ray magnetic scattering with polarization analysis. In general, the magnetic scattering intensities are given by:^{47,50}

$$I \propto \frac{1}{\mu^* \sin(2\theta)} \left| \sum_n f_n^{XRES}(\vec{k}, \hat{\epsilon}, \vec{k}', \hat{\epsilon}') e^{i\vec{Q} \cdot \vec{R}_n} \right|^2, \quad (1)$$

$$f_{nE1}^{XRES} \propto \begin{bmatrix} 0 & \hat{k}' \cdot \hat{z}_n \\ -\hat{k}' \cdot \hat{z}_n & (\hat{k} \times \hat{k}') \cdot \hat{z}_n \end{bmatrix} \propto \begin{bmatrix} 0 & z_1 \cos\theta + z_3 \sin\theta \\ -z_1 \cos\theta + z_3 \sin\theta & -z_2 \sin(2\theta) \end{bmatrix}, \quad (2)$$

where θ is the Bragg angle, z_1 , z_2 and z_3 are the components of the magnetic moment at the n th site, according to the commonly used geometry convention of Ref. 52; σ , π , σ' and π' describe the incident (non-primed terms) and scattered (primed) photon polarizations.

As described previously, two experimental setups have been used in this work, in the vertical (4-ID-D beamline) and horizontal (ID-20) scattering configurations. This permitted us to access all four polarization channels of the 2x2 matrix in (2) and to determine the magnetic moment orientations through their polarization dependence at the $E1$ resonance by comparing the relative intensities of experimental $(\frac{1}{2}, 0, l)$ magnetic peaks with the calculated ones using the appropriate terms of matrix (2).⁵⁰

In the case of Sm₂IrIn₈ the magnetic propagation vector $\vec{\eta} = (\frac{1}{2}, 0, 0)$ does not unequivocally determine the magnetic structure due to the presence of two magnetic Sm atoms per chemical unit cell along the \hat{c} direction. Therefore, as stated above, we have an antiparallel ordering of the Sm moments along the \hat{a} direction and a parallel ordering along \hat{b} . Along \hat{c} there are, however, two possibilities of coupling that can take place: a parallel arrangement (Model I), in which the moments of neighboring Sm ions along c axis are parallel to each other (sequence ++ ++ ++ ...), or the antiparallel coupling (Model II), with the sequence (+- +- +- ...). These two possibilities have been considered into the calculated magnetic structure factor while orienting the magnetic moment along the three crystallographic directions for five different $(\frac{1}{2}, 0, l)$ magnetic Bragg peaks, with $l = 6, 7, 8, 9, 10$. The calculated intensities are strongly dependent on the projections of magnetic moments along the crystallographic axis through the product $\hat{k}' \cdot \hat{z}_n$ of equation (2). Therefore, they were compared to the relative observed intensities for each case. This evaluation was performed at the vertical geometry of the 4-ID-D

where μ^* is the absorption correction for asymmetric reflections, 2θ is the scattering angle, $\vec{Q} = \vec{k}' - \vec{k}$ is the wave-vector transfer, \vec{k} and \vec{k}' ($\hat{\epsilon}$ and $\hat{\epsilon}'$) are the incident and scattered wave (polarization) vectors, respectively. \vec{R}_n is the position of the n th resonant atom in the lattice, and \hat{z}_n is the moment direction of this atom. The resonant scattering amplitude contains both dipole ($E1$) and quadrupole ($E2$) contributions. For the determination of the magnetic structure of this work we have used the second term of the electric dipole transition ($E1$) form factor which produces magnetic peaks. In this case we have:

beamline at 9 K by performing rocking scans with the crystal analyzer and numerically integrating the data.⁵⁰ We show this analysis in Table I, where “Model I” stands for the ++ ++ ++ ... sequence and “Model II” for the +- +- +- ... one. This comparison shows that the model which best fits the experimental data is the one assuming antiparallel coupling along c axis (Model II) with the magnetic moments approximately oriented along the a axis (according to matrix (2), for a σ polarized incident beam and peaks at reciprocal space positions with the (001) normal surface contained in the scattering plane, contributions from an oriented moment along \hat{b} direction cannot be detected).

In addition, we have also measured the $\pi - \sigma'$ and $\pi - \pi'$ polarization channels at the horizontal geometry of the ID-20 beamline. Measuring these two channels we gained access to the z_1 and z_3 components (in equation 2) of magnetic moment vector in one case [$\pi - \sigma'$, Figure 3(a)] and to z_2 in the other [$\pi - \pi'$, Figure 3(b)]. There is a clear indication that for the $\pi - \sigma'$ channel the observed data are well fit when considering the moments along the \hat{a} direction [dotted curve in Figure 3(a)] instead of \hat{c} direction [short dashed curve]. Also in this case the $E1$ terms are not sensitive to the component of the ordered moment perpendicular to the scattering plane, i.e. along b axis. Further, when measuring the channel ($\pi - \pi'$) we are only allowed to measure the b component, which is confirmed by the good fit of experimental data when assuming magnetic moments along such direction [dash-dotted curve in Figure 3(b)]. These two last results indicate that the Sm moments actually have components along both a and b real space axis and not perfectly aligned along any of these two directions.

To determine the exact orientation of the magnetic moments within the ab plane, we have performed azimuthal scans (ϕ scan) through the $(\frac{1}{2}, 0, 9)$ reflection (Figure 4)

TABLE I: Comparison between observed and calculated intensities of magnetic Bragg reflections, assuming either parallel (model I) or antiparallel (model II) alignment between the moments of two Sm ions along the c axis in the same chemical unit cell.

(h, k, l)	Exp. Data	MODEL I		MODEL II	
		\mathbf{m}/c	\mathbf{m}/a	\mathbf{m}/c	\mathbf{m}/a
(1/2,0,6)	66	13	29	24	55
(1/2,0,7)	78	17	29	39	68
(1/2,0,8)	5	77	100	3.4	4.5
(1/2,0,9)	100	3	3	100	100
(1/2,0,10)	12	100	68	32	23

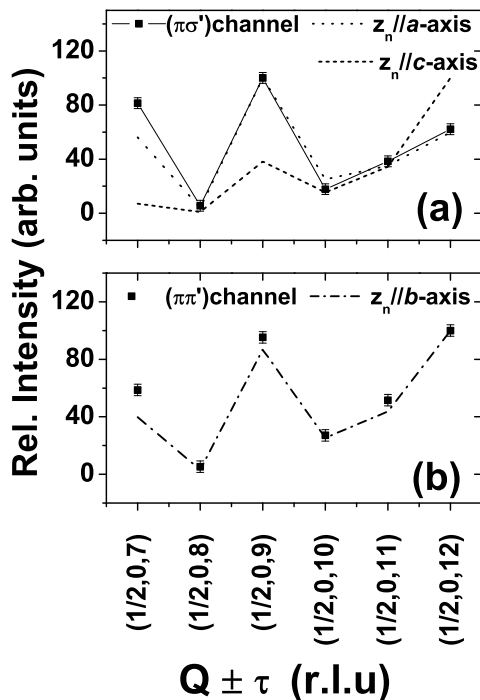


FIG. 3: Analysis of the possible magnetic moment directions for Sm_2IrIn_8 at the L_2 resonance. \mathbf{Q} -dependence of the integrated intensities of: (a) six satellite peaks signal in the $\pi - \sigma'$ channel with the moments along \hat{a} and \hat{c} , and (b) in the $\pi - \pi'$ with moments parallel to \hat{b} .

at the $E1$ resonance. At the $\sigma - \pi'$ polarization channel this procedure warrants the determination of moments directions with no ambiguity because the magnetic cross section is strongly dependent of the magnetic moment direction and the polarization of the incoming and scattered radiation, the maximum (minimum) intensity in the curve will occur with the magnetic moment being parallel (perpendicular) to the diffraction plane. With the experimental setup of 4-ID-D beamline we had access to record points at azimuthal angles ϕ between -50°

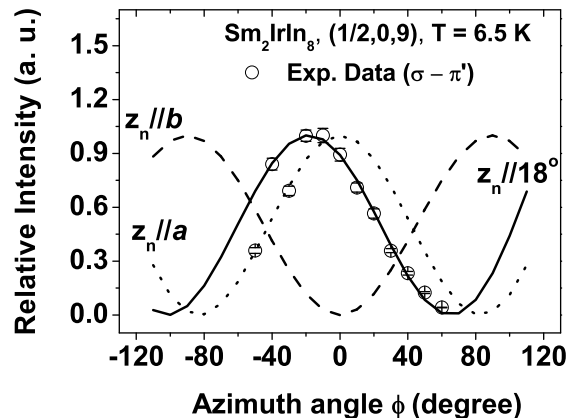


FIG. 4: Azimuth scan analysis. Normalized integrated intensities of the $(\frac{1}{2}, 0, 9)$ magnetic peak at $T = 6.5$ K (open circles). The other curves represent the integrated intensities behavior considering the magnetic moments along the \hat{a} (dotted line), \hat{b} (dashed) and 18° away from \hat{a} (solid line) direction.

and 60° . In order to compare with the observed data, one can calculate the intensities for the $\sigma - \pi'$ channel using the expressions (1) and (2) and a reasonably simple geometry analysis considering the projections of both \hat{k}' and \hat{z}_n on the coordinate system of Ref. 52 when the azimuth angle is changed. Then, the calculated intensity is proportional to $I^{\sigma\pi'} \propto |-\cos\theta \cos\phi \cos\alpha + \sin\theta \sin\alpha|^2$, where α represents the assymetry angle between the scattering and the normal surface vector.⁵⁰ Figure 4 shows the experimental and the calculated relative intensities considering the moment along the a and b axis, as well as 18° tilted from the a axis, which is the value that nicely adjust the experimental data. Considering the experimental errors we can then conclude that the magnetic moment is in the ab plane making $(18^\circ \pm 3^\circ)$ with the \hat{a} direction of the sample. Using all the above results, a model of the magnetic unit cell of Sm_2IrIn_8 can be constructed and is shown in Figure 5.

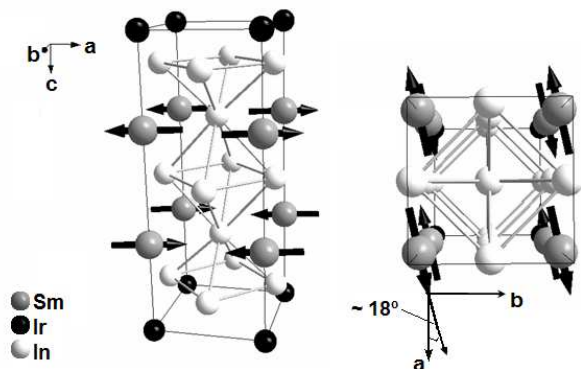


FIG. 5: Magnetic structure of Sm_2IrIn_8 below $T_N = 14.2$ K (left) and a Sm-In plane top view (right) showing the in-plane arrangement of Sm moments.

As it was observed in the magnetic structure of other members of the $R_m\text{MIn}_{3m+2}$ series such as NdRhIn_5 ³⁸, TbRhIn_5 ,⁷ GdRhIn_5 ,⁴¹ and Gd_2IrIn_8 ³⁶ the magnetic structure of Sm_2IrIn_8 presents a lower symmetry than the crystallographic structure, as the Sm spins present different relative orientations along the \hat{a} and \hat{b} directions even though a and b are indistinguishable. This spin arrangement was explained by considering the first (J_1) and second (J_2) R-neighbors exchange interactions in the case of a small J_1/J_2 ratio.⁴¹

Considering the observation of this kind of magnetic structure in tetragonal compounds, it may be expected that at zero magnetic field the antiferromagnetic ordering takes place with the formation of antiferromagnetic domains where the relative orientation of the magnetic moments along a given direction (\hat{a} or \hat{b}) changes from parallel to antiparallel between the domains. The presence of a twinned magnetic structure with symmetry-related domains was evidenced by the observation of both $(\frac{1}{2}, 0, l)$ and $(0, \frac{1}{2}, l)$ reflection-types in this work. To further investigate the presence of antiferromagnetic domains in the ordering state of Sm_2IrIn_8 we follow the behavior of the magnetic $(\frac{1}{2}, 0, l)$ and $(0, \frac{1}{2}, l)$ reflections under an applied magnetic field.

Figure 6 presents the behavior of the $(\frac{1}{2}, 0, 9)$ and $(0, \frac{1}{2}, 9)$ intensities as a function of the applied magnetic field of 10 T along one of the tetragonal axis in the plane (defined as \hat{b} direction). At zero field and $T = 6$ K, both $(\frac{1}{2}, 0, 9)$ [open circles] and $(0, \frac{1}{2}, 9)$ [closed squares] intensities can be observed with comparable magnitude [Figure 6(a)]. The $(\frac{1}{2}, 0, 9)$ intensity is roughly 66% that of the $(0, \frac{1}{2}, 9)$ peak. The sample was then field cooled ($H = 10$ T) from the paramagnetic (16 K) to the ordered state (6 K) with the field applied along the \hat{b} direction. As can be seen in Figure 6(b) the $(0, \frac{1}{2}, 9)$ diffraction peak disappears as the magnetic field favors the parallel spin orientation along the b axis. The same effect was also observed for the other five $(0, \frac{1}{2}, l)$ reflections (not shown). The results under applied magnetic field shown in Fig-

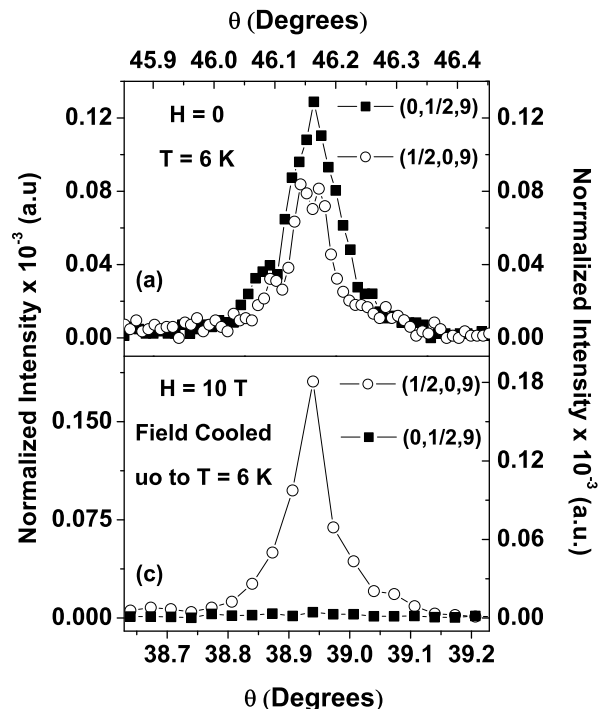


FIG. 6: Field-dependence of the integrated intensities of the $(\frac{1}{2}, 0, 9)$ and $(0, \frac{1}{2}, 9)$ magnetic peaks taken with transverse (θ) scans around each reciprocal space lattice points. (a) For $H = 0$ applied field at $T = 6$ K, (b) for $H = 10$ T and (c) field cooled from 16 K to 6 K at $H = 10$ T.

ure 6 confirm the existence of a twinned magnetic structure for Sm_2IrIn_8 which allows the observation of both $(0, \frac{1}{2}, l)$ and $(\frac{1}{2}, 0, l)$ magnetic reflections at zero field.

IV. DISCUSSION

Early studies on the antiferromagnetic cubic compound SmIn_3 have shown multiple magnetic transitions associated with quadrupolar ordering, magnetoelastic and magnetocrystalline competitive effects at 14.7, 15.2 and 15.9 K (the former two temperatures being associated with successive magnetic dipolar, antiferromagnetic, orders and the last one due to quadrupolar ordering).^{42,43} For the tetragonal Sm_2IrIn_8 , the insertion of two additional SmIn_3 atomic layers into the crystalline structure slightly decreases T_N compared to that of SmIn_3 (14.2 and 15.2 K for the Sm2-1-8 and Sm1-0-3 T_N 's, respectively) and an additional anomaly at 11.5 K has been observed in the specific heat and resistivity measurements,⁵ probably related to the successive transitions seen in the ordered phase of the SmIn_3 .

Following the investigation of the isostructural magnetic non-Kondo compounds from the $R_m\text{MIn}_{3m+2}$ family, where the details the $4f$ magnetism along the series may be important to understand the possible magnetic-

mediated superconductivity in the compounds with $R = \text{Ce}$, we have studied the magnetic structure of Sm_2IrIn_8 , which is the only compound from this family with a clear first order antiferromagnetic transition and now it is the first Sm-member from this family with a solved magnetic structure, which is the main result of this work. The determination of the Sm2-1-8 magnetic structure allows for the investigation of the CEF driven trends of magnetic properties within the $\text{R}_m\text{MIn}_{3m+2}$ family to be extended to the Sm-based members.

Our results confirm the complex resonance profile of Sm-based compounds (at one satellite reciprocal point, Figure 2), as seen in previous studies of pure Sm.⁴⁵ It has been argued that the larger intensity of $E2$ resonance at Sm L_3 edge compared to its intensity at the L_2 edge may be explained qualitatively by the spin-orbit splitting of the intermediate $4f$ levels involved.⁴⁵ The L_3 transitions connect the $j = \frac{7}{2}$ state while L_2 involves transitions to the $j = \frac{5}{2}$ level, which lie lower in energy and therefore can be preferentially populated by the five $4f$ Sm electrons. This reduces the number of vacant $j = \frac{5}{2}$ states from 6 to 1, in contrast to the 8 states available for the $j = \frac{7}{2}$ level, which increases the transition probability of the $E2$ resonance at Sm L_3 in Sm_2IrIn_8 .

Considering the additional magnetic transitions observed for SmIn_3 ,^{42,43} and the additional anomaly at $T = 11.5$ K in heat capacity and electrical resistivity measurements for Sm_2IrIn_8 ,³⁷ we did not observe any discontinuities, within the resolution of our experiment, in the integrated intensities of the $(0, \frac{1}{2}, 9)$ magnetic peak from roughly 4 K up to 16 K (Figure 1). Therefore we conclude that there are no changes of the magnetic propagation vector $\vec{\eta} = (\frac{1}{2}, 0, 0)$ below T_N . For completeness, on going field-dependent heat capacity and thermal expansion measurements (not shown and will be published elsewhere) have revealed no field-induced transitions up to $H=9$ and 18 T, respectively, similarly to SmIn_3 where no additional transition was found with applied field up to $H=32$ T.⁴⁴

On the other hand, recent works have shown that the low temperature CEF configuration plays a fundamental role on the behavior of T_N and the magnetic moment directions within the $\text{R}_m\text{MIn}_{3m+2}$ family.^{7,32,37,40} Further, Kubo *et al.*⁵³ has also proposed an orbital controlled mechanism for superconductivity in the Ce-based compounds from this family. For the Sm members, CEF effects confine the magnetic moments to the ab plane, consistent with the experimental CEF trends observed for $R = \text{Ce}, \text{Nd}$ and Tb ^{5,6,7,32} and also by the predictions of a recently developed mean field theoretical model.^{7,37} If the magnetic ordered moments lie in the ab -plane but they are more magnetically susceptible along the c axis the magnetic order can be frustrated to lower T_N values than for their cubic relatives. The mean-field model of Ref. 37, however, only includes the contributions of tetragonal CEF and first neighbor isotropic dipolar exchange interaction. Therefore, it may not be expected to work for Sm containing compounds, because for the

Sm^{3+} ion the first excited J -multiplet lying just above the ground state is closer in energy. Thus, the tetragonal CEF splitting can mix both the excited and ground state CEF scheme and this particular effect should be considered into the calculations. Indeed, this is the responsible for the non-linear response of the inverse of magnetic susceptibility at high temperatures on SmIn_3 and other Sm-based compounds,^{11,54} as well as in Sm_2IrIn_8 .⁵ Furthermore, as it was found for SmIn_3 ,^{42,43} quadrupolar magnetic interactions also have to be considered in order to achieve a complete description of the magnetic properties of the Sm-based compounds in the $\text{R}_m\text{MIn}_{3m+2}$ family.

Apart from the higher complexity of the magnetic properties of the Sm-compounds, it was found experimentally that T_N is decreased (roughly $\sim 10\%$) for the tetragonal compounds when compared to the cubic SmIn_3 . In addition, we have found that the magnetic structure of Sm_2IrIn_8 shows the ordered Sm moments in the ab plane, as expected in the case of T_N suppression.^{7,37} Although the changes in T_N for the Sm compounds are much smaller (perhaps due to the particularities of the Sm^{3+} ion discussed above) than that observed for $R = \text{Ce}, \text{Nd}$ and Tb in the $\text{R}_m\text{MIn}_{3m+2}$ family, we can conclude with the solution of the magnetic structure reported here, that the general CEF trend of the $\text{R}_m\text{MIn}_{3m+2}$ is also qualitatively present in Sm_2IrIn_8 .

V. CONCLUSION

In summary, we have presented the results of the magnetic structure determination of the intermetallic antiferromagnet Sm_2IrIn_8 . The magnetic order is commensurate with propagation vector $\vec{\eta} = (\frac{1}{2}, 0, 0)$ and the Sm moments oriented in the ab plane. We used different scattering geometries (exploring the polarization dependences of magnetic intensities) and azimuthal scans around a magnetic reciprocal space point to determine without ambiguity that the moments are aligned approximately 18° away from the a axis. The temperature behavior of the magnetic satellites have been probed at the $(0, \frac{1}{2}, 9)$ reciprocal node and show no evidence of changes in the magnetic structure within the studied temperature range. Besides, an abrupt (non-power law) decrease of magnetic intensities at T_N was found, consistent with the first order character of the antiferromagnetic transition of Sm_2IrIn_8 . The resonance properties at the Samarium L_2 and L_3 absorption edges revealed both resonant $E1$ and $E2$ process with roughly one order of magnitude more intense resonance peaks at the L_2 edge and a much stronger quadrupole resonance in the L_3 edge. The orientation of Sm moments in the ab plane and the small decrease of T_N compared to its value for SmIn_3 agrees with a general CEF trend found in the $\text{R}_m\text{MIn}_{3m+2}$ family.

Acknowledgments

This work was supported by FAPESP (SP-Brazil) Grants No. 05/55272-9, 05/00962-0, 04/08798-2 and 03/09861-7, CNPq (Brazil) Grants No. 307668/03, 04/08798-2, 304466/20003-4 and 140613/2002-1, and FAEPEX (SP-Brazil) Grant No. 633/05. Use of

the Advanced Photon Source was supported by the U. S. Department of Energy, Office of Science, Office of Basic Energy Sciences, under Contract No. DE-AC02-06CH11357. The staff at the 4-ID-D and ID-20 beam lines are gratefully acknowledged for providing an outstanding scientific environment during these experiments.

-
- * Electronic address: cadriano@ifi.unicamp.br
- ¹ H. Hegger, C. Petrovic, E. G. Moshopoulou, M. F. Hundley, J. L. Sarrao, Z. Fisk, and J. D. Thompson, *Phys. Rev. Lett.* **84**, 4986 (2000).
 - ² C. Petrovic, R. Movshovich, M. Jaime, P. G. Pagliuso, M. F. Hundley, J. L. Sarrao, J. D. Thompson, and Z. Fisk, *Europhys. Lett.* **354-359**, 4986 (2001).
 - ³ C. Petrovic, P. G. Pagliuso, M. F. Hundley, R. Movshovich, J. L. Sarrao, J. D. Thompson, Z. Fisk, and P. Monthoux, *J. Phys.: Condens. Matter* **13**, L337 (2001).
 - ⁴ J. D. Thompson, R. Movshovich, Z. Fisk, F. Bouquet, N. J. Curro, R. A. Fisher, P. C. Hammel, H. Hegger, M. F. Hundley, M. Jaime, et al., *J. Magn. Magn. Mat.* **226-230**, 5 (2001).
 - ⁵ P. G. Pagliuso, J. D. Thompson, M. F. Hundley, J. L. Sarrao, and Z. Fisk, *Phys. Rev. B* **63**, 054426 (2001).
 - ⁶ P. G. Pagliuso, J. D. Thompson, M. F. Hundley, and J. L. Sarrao, *Phys. Rev. B* **62**, 12266 (2000).
 - ⁷ R. Lora-Serrano, C. Giles, E. Granado, D. J. Garcia, E. Miranda, O. Agüero, L. M. Ferreira, J. G. S. Duque, and P. G. Pagliuso, *Phys. Rev. B* **74**, 214404 (2006).
 - ⁸ G. Chen, S. Ohara, M. Hedo, Y. Uwatoko, K. Saito, M. Sorai, and I. Sakamoto, *J. Phys. Soc. Japan* **71**, 2836 (2002).
 - ⁹ E. G. Moshopoulou, Z. Fisk, J. L. Sarrao, and J. D. Thompson, *J. Solid State Chem.* **158**, 25 (2001).
 - ¹⁰ E. G. Moshopoulou, R. M. Ibberson, J. L. Sarrao, J. D. Thompson, and Z. Fisk, *Acta Crystallographica B* **62**, 173 (2006).
 - ¹¹ K. H. J. Buschow, H. W. de Wijn, and A. M. van Diepen, *J. Chem. Phys.* **50**, 137 (1969).
 - ¹² P. G. Pagliuso, C. Petrovic, R. Movshovich, D. Hall, M. F. Hundley, J. L. Sarrao, J. D. Thompson, and Z. Fisk, *Phys. Rev. B* **64**, 100503(R) (2001).
 - ¹³ P. G. Pagliuso, R. Movshovich, A. D. Bianchi, M. Nicklas, J. D. Thompson, M. F. Hundley, J. L. Sarrao, and Z. Fisk, *Physica B* **312-313**, 129 (2002).
 - ¹⁴ L. D. Pham, T. Park, S. Maquilon, J. D. Thompson, and Z. Fisk, *Phys. Rev. Lett.* **97**, 056404 (2006).
 - ¹⁵ V. S. Zapf, E. J. Freeman, E. D. Bauer, J. Petricka, C. Sirvent, N. A. Frederick, R. P. Dickey, and M. B. Maple, *Phys. Rev. B* **65**, 014506 (2002).
 - ¹⁶ T. Park, F. Ronning, H. Q. Yuan, M. B. Salamon, R. Movshovich, J. L. Sarrao, and J. D. Thompson, *Nature* **440**, 65 (2006).
 - ¹⁷ V. A. Sidorov, M. Nicklas, P. G. Pagliuso, J. L. Sarrao, Y. Bang, A. V. Balatsky, and J. D. Thompson, *Phys. Rev. Lett.* **89**, 157004 (2002).
 - ¹⁸ A. Bianchi, R. Movshovich, I. Vekhter, P. G. Pagliuso, and J. L. Sarrao, *Phys. Rev. Lett.* **91**, 257001 (2003).
 - ¹⁹ E. D. Bauer, C. Capan, F. Ronning, R. Movshovich, J. D. Thompson, and J. L. Sarrao, *Phys. Rev. Lett.* **94**, 047001 (2005).
 - ²⁰ J. Paglione, M. A. Tanatar, D. G. Hawthorn, E. Boaknin, R. W. Hill, F. Ronning, M. Sutherland, L. Taiterfer, C. Petrovic, and P. C. Canfield, *Phys. Rev. Lett.* **91**, 246405 (2003).
 - ²¹ R. S. Kumar and J. L. S. A. L. Cornelius, *Phys. Rev. B* **70**, 214526 (2004).
 - ²² N. Oeschler, P. Gegenwart, M. Lang, R. Movshovich, J. L. Sarrao, and J. D. T. F. Steglich, *Phys. Rev. Lett.* **91**, 076402 (2003).
 - ²³ A. D. Christianson, E. D. Bauer, J. M. Lawrence, P. S. Riseborough, N. O. Moreno, P. G. Pagliuso, J. L. Sarrao, J. D. Thompson, E. A. Goremychkin, F. R. Trouw, et al., *Phys. Rev. B* **70**, 134505 (2004).
 - ²⁴ N. Harrison, U. Alver, R. G. Goodrich, I. Vekhter, J. L. Sarrao, P. G. Pagliuso, N. O. Moreno, L. Balicas, Z. Fisk, D. Hall, et al., *Phys. Rev. Lett.* **93**, 186405 (2004).
 - ²⁵ S. Raj, Y. Iida, S. Souma, T. Sato, T. Takahashi, H. Ding, S. Ohara, T. Hayakawa, G. F. Chen, I. Sakamoto, et al., *Phys. Rev. B* **71**, 224516 (2005).
 - ²⁶ D. Hall, E. C. Palm, T. P. Murphy, S. W. Tozer, Z. Fisk, U. Alver, R. G. Goodrich, J. L. Sarrao, P. G. Pagliuso, and T. Ebihara, *Phys. Rev. B* **64**, 212508 (2001).
 - ²⁷ D. Hall, E. C. Palm, T. P. Murphy, S. W. Tozer, C. Petrovic, E. Miller-Ricci, L. Peabody, C. Q. H. Li, U. Alver, R. G. Goodrich, et al., *Phys. Rev. B* **64**, 064506 (2001).
 - ²⁸ J. Costa-Quintana and F. López-Aguilar, *Phys. Rev. B* **67**, 132507 (2003).
 - ²⁹ J. L. Sarrao, L. A. Morales, J. D. Thompson, B. L. Scott, G. R. Stewart, F. Wastin, J. Rebizant, P. Boulet, E. Colineau, and G. H. Lander, *Nature* **420**, 297 (2002).
 - ³⁰ E. D. Bauer, J. D. Thompson, J. L. Sarrao, L. A. Morales, F. Wastin, J. Rebizant, J. C. Griveau, P. Javorsky, P. Boulet, E. Colineau, et al., *Phys. Rev. Lett.* **93**, 147005 (2004).
 - ³¹ A. D. Christianson, A. Llobet, W. Bao, J. S. Gardner, I. P. Swainson, J. W. Lynn, J.-M. Mignot, K. Prokes, P. G. Pagliuso, N. O. Moreno, et al., *Phys. Rev. Lett.* **95**, 217002 (2005).
 - ³² R. Lora-Serrano, L. M. Ferreira, D. J. Garcia, E. Miranda, C. Giles, J. G. S. Duque, E. Granado, and P. G. Pagliuso, *Physica B* **384**, 326 (2006).
 - ³³ N. V. Hieu, H. Shishido, T. Takeuchi, A. Thamizhavel, H. Nakashima, K. Sugiyama, R. Settai, T. D. Matsuda, Y. Haga, M. Hagiwara, et al., *J. Phys. Soc. Japan* **75**, 074708 (2006).
 - ³⁴ A. Malinowski, M. F. Hundley, N. O. Moreno, P. G. Pagliuso, J. L. Sarrao, and J. D. Thompson, *Phys. Rev. B* **68**, 184419 (2003).
 - ³⁵ V. F. Correa, L. Tung, S. M. Hollen, P. G. Pagliuso, N. O. Moreno, J. C. Lashley, J. L. Sarrao, and A. H. Lacerda,

- Phys. Rev. B **69**, 174424 (2004).
- ³⁶ E. Granado, P. G. Pagliuso, C. Giles, R. Lora-Serrano, F. Yokaichiya, and J. L. Sarrao, Phys. Rev. B **69**, 144411 (2004).
- ³⁷ P. G. Pagliuso, D. J. Garcia, E. Miranda, E. Granado, R. Lora-Serrano, C. Giles, J. G. S. Duque, R. R. Urbano, C. Rettori, J. D. Thompson, et al., J. Appl. Phys. **99**, 08P703 (2006).
- ³⁸ Wei Bao, P. G. Pagliuso, J. L. Sarrao, J. D. Thompson, Z. Fisk, J. W. Lynn, and R. W. Erwin, Phys. Rev. B **62**, R14621 (2000); *ibid.* **63**, 219901 (E) (2001).
- ³⁹ W. Bao, P. G. Pagliuso, J. L. Sarrao, J. D. Thompson, Z. Fisk, and J. W. Lynn, Phys. Rev. B **64**, 020401(R) (2001).
- ⁴⁰ S. Chang, P. G. Pagliuso, W. Bao, J. S. Gardner, I. P. Swainson, J. L. Sarrao, and H. Nakotte, Phys. Rev. B **66**, 132417 (2002).
- ⁴¹ E. Granado, B. Uchoa, A. Malachias, R. Lora-Serrano, P. G. Pagliuso, and H. W. Jr., Phys. Rev. B **74**, 214428 (2006).
- ⁴² M. Kasaya, B. Liu, M. Sera, T. Kasuya, D. Endoh, T. Goto, and F. Fujimura, J. Magn. Magn. Mater. **52**, 289 (1985).
- ⁴³ D. Endoh, T. Goto, A. Tamaki, B. Liu, M. Kasaya, T. Fujimura, and T. Kasuya, J. Phys. Soc. Jpn **58**, 940 (1989).
- ⁴⁴ Z. Kletowski, J. Magn. Magn. Mater. **186**, L7 (1998).
- ⁴⁵ A. Stunault, K. Dumesnil, C. Dufour, C. Vettier, and N. Bernhoeft, Phys. Rev. B **65**, 064436 (2002).
- ⁴⁶ Z. Fisk and J. P. Remeika, in *Handbook on the Physics and Chemistry of Rare Earths*, edited by J. K. A. Gschneider and E. L. Eyring (Elsevier, North-Holland, 1989), vol. 12, p. 53.
- ⁴⁷ J. P. Hill and D. F. McMorrow, Acta Crystallogr. **A52**, 236 (1996).
- ⁴⁸ A. Zheludev, J. P. Hill, and D. J. Buttrey, Phys. Rev. B **54**, 7216 (1996).
- ⁴⁹ J. P. Hill, A. Vigliante, D. Gibbs, J. L. Peng, and R. L. Greene, Phys. Rev. B **52**, 6575 (1995).
- ⁵⁰ C. Detlefs, A. H. M. Z. Islam, A. I. Goldman, C. Stassis, P. C. Canfield, J. P. Hill, and D. Gibbs, Phys. Rev. B **55**, R680 (1997).
- ⁵¹ J. P. Hannon, G. T. Trammell, M. Blume, and D. Gibbs, Phys. Rev. Lett. **61**, 1245 (1988).
- ⁵² M. Blume and D. Gibbs, Phys. Rev. B **37**, 1779 (1988).
- ⁵³ K. Kubo and T. Hotta, J. Phys. Soc. Japan **75**, 083702 (2006).
- ⁵⁴ T. Tsuchida and W. E. Wallace, J. Chem. Phys. **43**, 3811 (1965).